Solid State Sciences 154 (2024) 107583

Contents lists available at ScienceDirect

Solid State Sciences

journal homepage: www.elsevier.com/locate/ssscie

Borides $Mn_{3-x}\{Rh,Ir\}_5B_2$ with $Ti_3Co_5B_2$-type: X-ray single crystal and TEM data, physical properties

Gerda Rogl [a], Markus Eiberger [a], Soner Steiner [a,b], Herwig Michor [b], Jiri Bursik [c], Gerald Giester [d], Andrij Grytsiv [a], Peter F. Rogl [a,*]

[a] Institute of Materials Chemistry, University of Vienna, Währingerstrasse 42, A-1090, Wien, Austria
[b] Institut of Solid State Physics, TU-Wien, Wiedner Hauptstrasse 8-10, A-1040, Wien, Austria
[c] Institute of Physics of Materials, Czech Academy of Sciences, Žižkova 22, CZ-61662, Brno, Czech Republic
[d] Institute of Mineralogy and Crystallography, University of Vienna, Josef-Holaubek-Platz 2, A-1090, Wien, Austria

ARTICLE INFO

Keywords:
Ternary borides
Crystal structure
TEM
Physical properties
Hardness

ABSTRACT

A cursory investigation of the phase relations in the Mn-{Rh,Ir}-B systems prompted for each system a ternary compound, $Mn_{3-x}\{Rh,Ir\}_5B_2$, the crystal structure of them was determined from X-ray single crystal data to be isotypic with the $Ti_3Co_5B_2$-type (space group *P4/mbm*, No. 127). In both cases the Mn-site in 2*a* at the origin of the unit cell exhibits a significant defect (or Mn/B substitution). Transmission electron microscopy studies confirm the absence of a superstructure related to these defects/disorder. The two phases, $Mn_{3-x}Rh_5B_2$ (x~0.34) and $Mn_{3-x}Ir_5B_2$ (x~0.85) at 950 °C show rather limited homogeneity regions pointing towards higher Mn-contents. Whereas temperature dependent magnetization and specific heat measurements of $Mn_{2.15}Ir_5B_2$ do not reveal any indication for a magnetic phase transition in the temperature range from 3 to 300 K, a broad specific heat anomaly at around 200 K and a tilde shape of the temperature dependent magnetization of $Mn_{2.66}Rh_5B_2$ appears indicative of an antiferromagnetic phase transition. The latter is also reflected by an anomaly of the electrical resistivity (ρ; 4–300 K) of $Mn_{2.66}Rh_5B_2$ which displays a non-monotonous temperature dependence, whereas ρ(T) of $Mn_{2.15}Ir_5B_2$ displays a simple metallic-like behavior dominated by scattering from defects. Elastic moduli and Poisson's ratio were determined at room temperature from Resonant Ultrasonic Spectroscopy (RUS) data yielding Young's moduli of E ~ 170 GPa for $Mn_{2.66}Rh_5B_2$ and E ~ 210 GPa for $Mn_{2.15}Ir_5B_2$. Vickers hardness HV is lower for $Mn_{2.66}Rh_5B_2$ (HV = 590 ≅ 5.79 GPa) than for $Mn_{2.15}Ir_5B_2$ (HV = 655 ≅ 6.42 GPa). The indentation fracture toughness for $Mn_{2.15}Ir_5B_2$ was $IK_C = 0.71 \pm 0.5$ MPa $m^{1/2}$.

1. Introduction

Metal borides have so far offered a surprisingly large variety of interesting physico-chemical properties covering hard (almost superhard and incompressible [1–5]) and wear resistant materials [6,7], permanent magnets with a still unsurpassed energy product [8,9], normal [10] to non-centrosymmetric heavy Fermion superconductivity [11–13] connected to quantum criticalities [14], re-entrant superconductivity in the interplay with magnetism [15] and many further features. Among the latter we need to mention recent use of borides as promising electrocatalysts for hydrogen production via water-splitting [16]. Besides all these highlights, boride materials crystallize in a wealth of structure types depending on boron aggregations as a function of the metal to boron ratio [17,18]. Particularly the magnetic interplay in borides has attracted increasing attention. Although among *3d* elements manganese is the one with the most intriguing magnetic features already in its pure modifications [19], little is known on the magnetic interactions in ternary boride compounds containing substantial amounts of Mn and even less information is available on the borides of Mn with the platinum metal group elements. One of the reasons for the obvious lack of information may be the adverse properties of the highly volatile manganese at elevated temperatures (vapour pressure of about 1 Torr–10^2 Pa at its melting point $T_m = 1246$ °C) and the even higher melting points of the binary, ternary and higher order borides. Thus, so far only minor amounts of Mn were incorporated in for instance $Hf_2Mn_{1-x}Ru_{5+x}B_2$ and $\{Ti,Hf\}_2MnCo_5B_2$ (both $Ti_3Co_5B_2$-structure type) [20–22] where a high magneto-crystalline anisotropy energy but weak inter-chain Mn–Mn spin exchange interactions have been calculated

---

* Corresponding author.
E-mail address: peter.franz.rogl@univie.ac.at (P.F. Rogl).

https://doi.org/10.1016/j.solidstatesciences.2024.107583
Received 29 October 2023; Received in revised form 27 May 2024; Accepted 28 May 2024

(DFT) for $Hf_2MnCo_5B_2$.

In view of the significant lacks in information, the present paper intends to shed light on (i) the formation of ternary Mn-{Ru,Os,Rh,Ir,Pd,Pt}-B compounds, (ii) the crystal structures adopted in the metal-rich part of the corresponding phase diagrams, and (iii) the physical properties of ternary compounds encountered in these diagrams. As a preliminary investigation of the diagrams Mn-{Ru,Os,Rh,Ir,Pd,Pt}-B revealed the formation of two borides $Mn_{3-x}\{Rh,Ir\}_5B_2$ the present paper will focus on these compounds. During the research work for this paper we became aware of a publication by B. Petermüller et al. [23] on the synthesis, crystal structure, and compressibility of $Mn_{3-x}Ir_5B_{2+x}$ ($0 \le x \le 0.5$; $B_0 = 209$ GPa, B' = 7.8 GPa) and Mn_2IrB_2. With respect to the crystal structure the two papers overlap but our investigation will also provide a complete characterization of the two compounds $Mn_{3-x}\{Rh,Ir\}_5B_2$ with respect to physical properties such as electrical resistivity, magnetic behavior, specific heat (all measured at low temperatures from ~2 to 300 K) as well as room temperature measurements of hardness and elastic moduli. In a future paper [24] the experimental studies will be complemented by density functional theory (DFT) calculations to elucidate the physical properties further including total relaxation, heat of formation, electronic density of states (chemical bonding) and band structure, vibrational properties, elastic constants C_{ij}, complemented by a Bader charge analysis.

2. Materials and methods

Samples (each of a mass of about 1 g) were prepared from 99.9 mass % pure powders of rhodium and iridium (Ögussa, Austria), and crystalline boron (99.95 %, H.C. Starck, D). Electrolytically deposited manganese (>99.95 %, Alfa Aesar, D) was in form of pieces, which were surface cleaned in concentrated HNO_3 prior to use. After the Mn-pieces were crushed to powder and blended with the other constituents in proper proportions, the powder mix was compacted in steel dies ($\Phi = 8$ mm, without lubricant) at a pressure of 50 kpf/mm^2. The compacted buttons were then melted in an arc furnace under 1 bar of Ti/Zr-gettered argon at least three times to ensure homogeneity. Weight losses due to the evaporation of manganese were compensated by adding about 3–5 mass% of the Mn content beforehand in order to keep the total mass loss of the sample after melting below 0.5 mass%. A part of each sample (within an Al_2O_3 crucible) was sealed in a silica capsule under 280 mbar Ar and heat treated at 950 °C for about 150 h and quenched. At maximum annealing temperature the Ar-pressure inside the silica capsule reached about 1 bar and efficiently suppressed Mn-evaporation.

All samples were characterized with respect to compositional analysis in as cast state and after annealing by Scanning Electron Microscopy (SEM), EPMA (electron probe microanalysis) on a Zeiss Supra 55 VP operated at 20 kV and 60 μA using EDX. As an accurate quantitative boron measurement is not possible by EPMA using EDX detection, we mainly focused on measuring the metal ratios. Precise lattice parameters and standard deviations were obtained by a least-squares refinement of room temperature Guinier-Huber X-ray powder data (XRD, Cu-$K_{\alpha 1}$) employing an internal standard of 99.9999 mass% pure Ge ($a_{Ge} = 0.5657906$ nm). For quantitative Rietveld refinements we applied the program FULLPROF [25].

Single crystal (SC) specimens of the borides $Mn_{3-x}\{Rh,Ir\}_5B_2$ suitable for X-ray structure determination were extracted from arc melted alloys with nominal composition (in at.%) Mn25{Rh,Ir}50B25 from which rather "spherical" single crystal fragments with "diameters" in the range of 30–70 μm were selected for X-ray analyses. They were inspected on an AXS D8-GADDS texture goniometer, which assured high crystal quality, unit cell dimensions and Laue symmetry of the single crystal specimens prior to X-ray intensity data collection at room temperature on a four-circle APEX II diffractometer equipped with a CCD area detector and an Incoatec Microfocus Source IμS (30 W, multilayer mirror, Mo-K_α; $\lambda = 0.071069$ nm; detector distance of 4 cm; full sphere; $2^\circ < 2\theta < 72^\circ$). Besides the general treatment of absorption effects using the multi-scan technique (SADABS [26]; redundancy of integrated reflections >6), no individual absorption correction was necessary because of the rather regular crystal shape and small dimensions of the investigated specimens (~50×60×70 μm^3). The crystal structure was solved applying direct methods (Program SHELXS-97) and refined against F^2 (Program SHELXL-97-2) within the program OSCAIL [27]. Finally, the crystal structure was standardized with the program TYPIX [28].

For TEM investigation a Philips CM12 STEM transmission electron microscope (TEM) operated at 120 kV with an EDAX EDX analyser was employed to get information about crystal symmetry and lattice parameters of selected phases. The samples for the TEM study were prepared in the form of thin lamellae (lateral dimensions about 10×7 μm^2) using a focused ion beam (FIB) technique in a TESCAN LYRA 3 XMU FEG/SEM × FIB scanning electron microscope.

The electrical resistivity measurement (error <3 %) from 4.2 K to room temperature was carried out in a conventional ^{4}He cryostat, employing an in-house equipment. The specific resistance was measured via a dc four-point technique employing a Lake Shore Resistance Bridge 370 AC, which measures voltage and temperature. Specific heat was measured in a Quantum Design PPMS in the temperature range from 2 to 320 K. Temperature and field dependent magnetization data were collected using a 6 T CRYOGENIC SQUID magnetometer.

Static hardness data were obtained from a microhardness tester, AD PAAR-MHT-4, mounted within a Zeiss Axioplan optical microscope. Vickers hardness values were calculated according to $HV = 1.891\ F/(2\ell)^2$, where F = 1 N is the load and 2ℓ is the diagonal length of the indent. At least 10 imprints per piece were conducted and evaluated to get the average value and respective error bars. The Young's modulus, E, was determined with RUS (Resonant Ultrasound Spectroscopy). This method uses cylindrical or cuboid samples, mounted "edge-to-edge" between two piezo-transducers, which are excited via a network analyser (HP 8751A) in the frequency range from 100 to 500 kHz till their eigenfrequency is reached. The so gained spectrum is fitted with a calculated one. Usually, the fit program yields E and Poisson's ratio ν. Fracture toughness is a measure of the resistance of a material to crack propagation. Vickers fracture resistance, which in the literature frequently is also called "indentation fracture toughness", IK_C, can be determined from the relation (eq. (1))

$$IK_C = \beta \left(\frac{E}{HV}\right)^{1/2} \frac{F}{c^{3/2}}, \qquad \text{(eq. 1)}$$

where E is the Young's modulus, HV is the hardness, F is the indentation load, c is the radial crack length from the center of the Vickers indentation and β is a function of the indenter angle, which for Vickers indentation is $\beta = 0.016(4)$. In this work indentation fracture resistance values were derived from the average of at least ten indentations at a load of 1 N employing the same equipment as for hardness tests.

3. Results and discussion

3.1. X-ray single crystal structure analysis of $Mn_{3-x}Rh_5B_2$ and $Mn_{3-x}Ir_5B_2$

From a preliminary investigation of the diagrams Mn-{Rh,Ir}-B, two borides, $Mn_{3-x}\{Rh,Ir\}_5B_2$, have been identified, for which single crystals could be isolated. The single crystal X-ray intensity patterns of both specimens (with Rh and Ir) were fully indexed on a tetragonal unit cell ($a \sim 0.92$ nm and $c \sim 0.28$ nm) revealing systematic X-ray extinctions (*0kl*) for $k \neq 2n$, (*h00*) for $h \neq 2n$, consistent with the centrosymmetric space group *P4/mbm* (#127) with the highest symmetry. X-ray single crystal structure solution and refinement rapidly converged to rather low values $R_{F2} \sim 0.070$ revealing rhodium (iridium) atoms in the crystallographic sites 2*c* (0,½,½) and 8*j* (x,y,½) with x~0.068; y~0.210 and Mn atoms in sites 4*g* (x,x+½,0) with x~0.176 and in 2*a* (origin of unit cell). At this stage the boron atoms are already clearly revealed in site 4*g* (x,x+½,0), x~0.63. Refinement with anisotropic displacement parameters (ADPs) for the metal atoms and isotropic parameters for boron finally yielded

Table 1a

Crystallographic data for $Mn_{3-x}\{Rh,Ir\}_5B_2$ from X-ray single crystal intensity data. $Ti_3Co_5B_2$-type; space group *P4/mbm*, No. 127, origin at centre; structure standardized with program *Structure Tidy* [28].

Parameter/compound	Crystal data	
Phase composition (EDX, at.%)	Mn27.7Rh51.9B21.8 [a]	Mn23.9Ir54.3B21.8 [a]
Refinement composition [at.%]	Mn27.5Rh51.8B20.7 ≡ $Mn_{3-x}Rh_5B_2$; x = 0.342	Mn23.5Ir54.7B21.8≡ $Mn_{3-x}Ir_5B_2$; x = 0.854
Structure type	defect $Ti_3Co_5B_2$-type	defect $Ti_3Co_5B_2$-type
θ range [deg.]	$2\leq 2\Theta \leq 80.6°$	$2\leq 2\Theta \leq 72.6°$
Crystal size	45 × 55 × 70 μm^3	50 × 65 × 70 μm^3
a = *b; c* [nm]	0.92186(1); 0.287802(5)	0.91267(2); 0.283213(7)
Linear absorption coeff. [mm^{-1}]	22.88	145.81
Density [Mg/m^3]	9.26	15.49
Reflections in refinement	$469 \geq 4\sigma(F_o)$ of 469	$356 \geq 4\sigma\ (F_o)$ of 356
Number of variables	20	20
Mosaicity	<0.49	<0.55
$R_{F2} = \Sigma\|F_o^2\text{-}F_c^2\|/\Sigma F_o^2$	0.0222	0.0252
w*R*2	0.0489	0.0537
R_{Int}	0.066	0.073
GOF	1.299	1.266
Extinction (Zachariasen)	0.032(1)	0.00081(1)
Mn1 in 2*a* (0, 0, 0)	occ = 0.657(8)	**Mn1** in 2*a*; occ = 0.146(21)
U_{11}=U_{22}; U_{33}; U_{23}=U_{13}=U_{12} = 0	0.0040(4); 0.0075(6)	0.0009(2); 0.0001(3)
Mn2 in 4*g* (x, x+½, 0); occ = 1	x = 0.17636(6)	**Mn2** in 4*g*, x = 0.1757(2); occ = 1
U_{11}=U_{22}; U_{33}; U_{23}=U_{13} = 0; U_{12}	0.0063(2); 0.0049(3); −0.0027(2)	0.0018(5); 0.0001(8); −0.0012(6)
Rh1 in 2*c* (0, ½, ½); occ = 1		**Ir1** in 2*c* (0, ½, ½); occ = 1
U_{11}=U_{22}; U_{33}; U_{23}=U_{13} = 0; U_{12}	0.0044(1); 0.0037(2); 0.0004(1)	0.0009(2); 0.0001(8); 0.0001(2)
Rh2 in 8*j* (x, y, ½); occ = 1	x = 0.06962(3); y = 0.21139(3)	**Ir2** in 8*j;* x = 0.06769(5); y = 0.20143(4); occ = 1
U_{11}; U_{22}; U_{33}; U_{23}=U_{13} = 0; U_{12}	0.065(1); 0.0106(1); 0.0088(1); 0.0028(1)	0.0025(2); 0.0033(2); 0.0015(2);0.0009(8)
B1 in 4*g* (x, x+½, 0); occ = 1	x = 0.6278(5)	**B1** in 4*g;* x = 0.6296(12); occ = 1
U_{iso}	0.0088(9)	0.001(2)
Principal mean square atomic displacements U_{ii}’		
Mn1	0.0075 0.0040 0.0040	0.0030 0.0006 0.0010
Mn2	0.0091 0.0049 0.0036	0.0069 0.0017 0.0017
Rh1/Ir1	0.0049 0.0040 0.0037	0.0011 0.0008 0.0005
Rh2/Ir2	0.0120 0.0088 0.0050	0.0038 0.0019 0.0015
Residual electron density;	2.10 (0.049 nm from Rh2);	13.8 (0.000 nm from Ir1);
max; min in ($electron/nm^3$) × 10^3	−2.05 (0.052 nm from Rh2)	−7.25(0.046 nm from Ir1)

[a] Boron content assumed to be at stoichiometric at.%.

$R_{F2} = 0.0222$ and residual electron densities less than $\pm\ 2.2\times10^3\ e/nm^3$ for the Rh compound but slightly higher values ($R_{F2} = 0.0252$, $13.8\times10^3\ e/nm^3$) for the heavy scatterer Ir. In both cases Mn-atoms in site 2*a* show a significantly reduced occupancy of occ = 0.657(8) (Rh-compound) and occ = 0.146(21) (Ir-compound), respectively. At this stage a test for missing symmetry via the ADDSYMM tool in program PLATON [29] confirmed the setting in space group *P*4/*mbm* with the highest symmetry. Partial occupancy in site 2*a* could also be a sign for possible superstructure formation. In agreement with careful inspection of the X-ray intensity data sets, which did not reveal any hints for faint superstructure reflections, selected area electron diffraction (SAED) patterns in Fig. 2 for both crystals and for different crystal orientations, obtained in TEM from thin lamellae, are fully consistent with the unit cell dimensions and exclude any supercell formation also for small crystal volumes. The SAED intensity simulations using the structure data in Table 1a were plotted in the JEMS software [30,31] and they are fully consistent with the observed patterns. Results of the crystal structure refinement are summarized in Table 1a. Both ratios Mn:Rh and Mn:Ir obtained from X-ray single crystal refinement, namely 34.8 : 65.2 and 30.0 : 70.0 for the Rh and Ir compounds, respectively, perfectly fit to the corresponding EPMA metal ratios of 34.7 : 65.3 and 30.6 : 69.4. A projection of the structure of $Mn_{3-x}Rh_5B_2$ is presented in Fig. 1 with the next nearest coordination figures for Mn1 atoms (cyan cubes) and for B-atoms (yellow triangular prisms). The nnn-coordination of the Mn2 atom is a pentagonal prism.

The structure refinements yield a defect structure, which, however, otherwise is fully ordered with two Mn sites, two platinum metal sites (Rh(Ir)) and one B site: this atom set corresponds to a Wyckoff sequence [28] of *127-jg²ca*. Search for isotypic compounds in Pearson’s Crystal Data [32] and the ICSD [33] data based on the lattice parameter and Wyckoff sequence yielded the structure type of $Ti_3Co_5B_2$, which proved

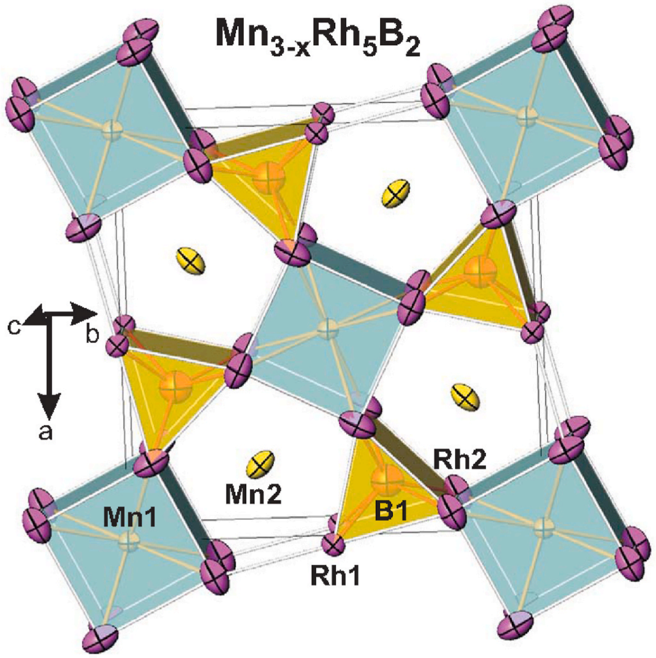

Fig. 1. Projection of the crystal structure of $Mn_{3-x}Rh_5B_2$ close to the *c*-axis. Atoms are presented with ADPs from single crystal refinement: Mn (gold), Rh (purple), B (red). Next nearest neighbor (nnn) coordination figures are outlined for Mn1 atoms (cyan cubes) and for B-atoms (yellow triangular prisms). The nnn-coordination of Mn2 atoms are pentagonal prisms.

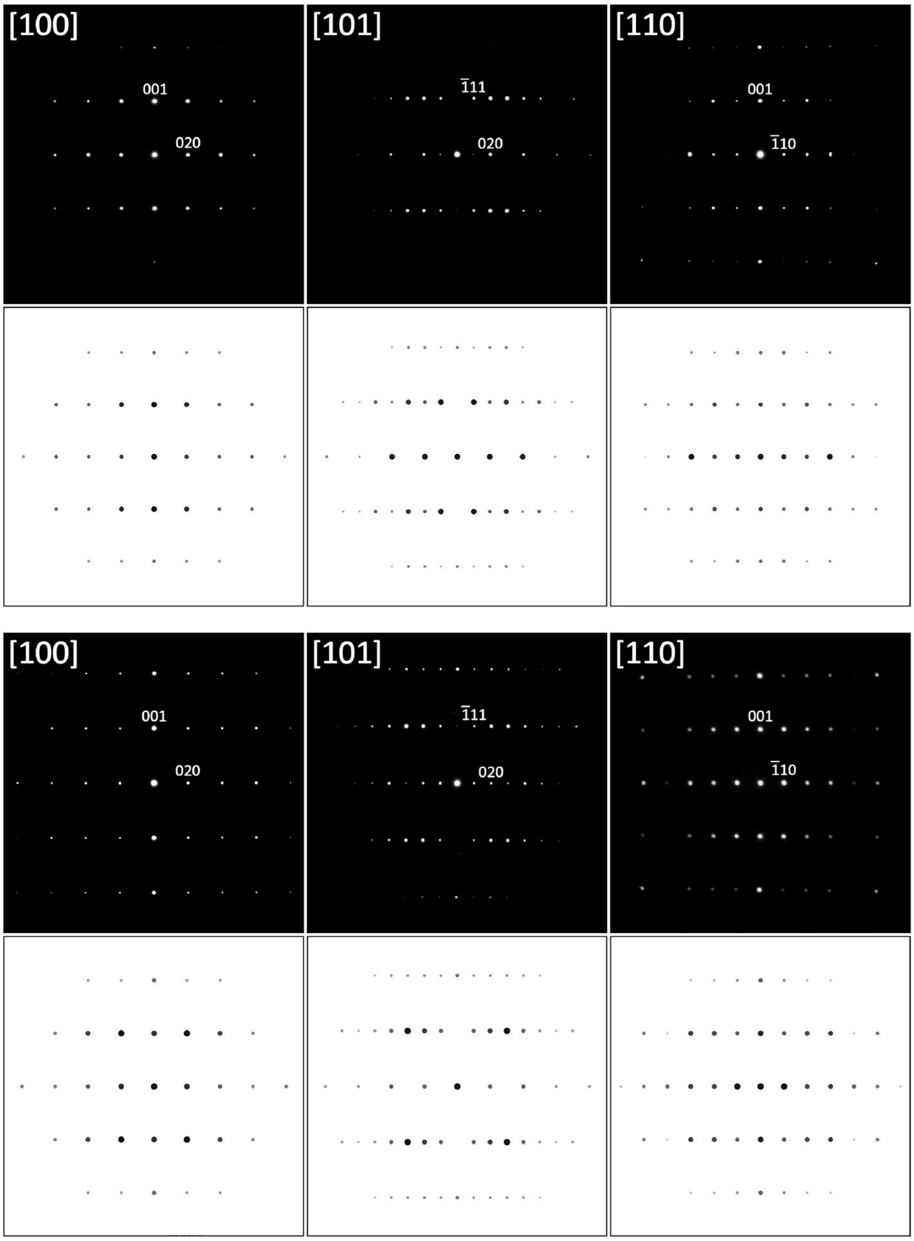

Fig. 2. Top Panel: SAED patterns of $Mn_{3-x}Rh_5B_2$ at various sample tilts together with results of simulation. Lower Panel: SAED patterns of $Mn_{3-x}Ir_5B_2$ at various sample tilts together with results of simulation. Weaker reflections *0k0* for $k \neq 2n$ observed in central horizontal line of [101] patterns are caused by dynamic effects (double diffraction), which are stronger in the Ir-containing sample.

to be the true prototype of both compounds $Mn_{3-x}\{Rh,Ir\}_5B_2$. Although first described by Y.P. Yarmolyuk and Yu.B. Kuzma in 1971 [34], the $Ti_3Co_5B_2$-type has been adopted in many ternary compounds in which the framework consisting of face-connected trigonal, tetragonal, and pentagonal prisms is formed by generally electron-rich and smaller transition metals such as Co, Rh, Ir, Ru, whereof the B atoms center the smaller trigonal prisms but relatively large atoms such as Mg, Sc, Ti, Zr, Hf, Nb are found to reside inside both the larger units, i.e. the tetragonal and pentagonal prisms. Whereas $Mn_{3-x}Rh_5B_2$ is a novel representative of the $Ti_3Co_5B_2$ type, $Mn_{3-x}Ir_5B_2$ has already been recently described by B. Petermüller et al. [23] with a slightly different formula $Mn_{3-x}Ir_5B_{2+x}$ ($0 \leq x \leq 0.5$). This difference comes from a random distribution of Mn/B in the 2*a* site in the structure model of Petermüller et al. [23].

Although boron atoms among boride structures have so far been extremely rare at the centers of metal cubes or cuboids, a recent experimental and theoretical study documented a continuous replacement of Ti- by B-atoms in $Ti_{3-x}Ru_{5-y}Ir_yB_{2+x}$ ($0 \leq x \leq 1$ and $1 < y < 3$; $Ti_3Co_5B_2$ type ref. [35]). We have tried already to refine Mn + B randomly in the 2*a* site, which yielded a mix of 0.602(4)Mn + 0.398B for $Mn_{2.6}Rh_5B_{2.4}$, and 0.030(4)Mn + 0.970B for the Ir-compound. Both refinements converged with indifferent atom parameters, R-values and residual peaks. We furthermore verified that occupation of the 2*a* site may in general be possible for (1) a random Mn-defect (as depicted in Table 1a,b), (2) a full random substitution by Mn + B (see above), or (3) simply a B-defect for $Mn_2Ir_5B_{2+x}$ (x almost 1). Even a random mix Mn + B + vacancy may be envisaged. Further DFT calculations [24] may provide a final conclusion.

Furthermore the homogeneity region of both phases $Mn_{3-x}\{Rh,Ir\}_5B_2$ extends in direction of more Mn so as to fill the 2*a* site. This observation is accompanied by only a small change in the B-concentration from 22 to 20 at.% but an increase in lattice parameters, which for instance for $Mn_{3-x}Ir_5B_2$ vary from $a = 0.91267(2)$ nm, $c = 0.283213(7)$ nm for x =

Table 1b
Interatomic distances for $Mn_{3-x}Rh_5B_2$; x = 0.343 and $Mn_{3-x}Ir_5B_2$; x = 0.854 (standard deviations for Rh-compound: <0.00006 nm for metals and <0.0007 nm for B; for Ir-compound: <0.00016 nm for metals and <0.0012 nm for B).

Atom	Neighbor	Distance	Atom	Neighbor	Distance
Mn1	8Rh2	0.2506	Mn1	8Ir2	0.2401
	2Mn1	0.2878		2Mn1	0.2832
Mn2	B1	0.2553	Mn2	B1	0.2513
	2Rh1	0.2712		2Ir1	0.2673
	4Rh2	0.2767		4Ir2	0.2747
	2Mn2	0.2878		2Mn2	0.2832
	4Rh2	0.2878		4Rh2	0.2863
B1	4Rh2	0.2134	B1	4Ir2	0.2169
	2Rh1	0.2202		2Ir1	0.2192
	(1Mn2	0.2553)		(1Mn2	0.2513)
Rh1	4B1	0.2202	Ir1	4B1	0.2192
	4Mn2	0.2712		4Mn2	0.2673
	4Rh2	0.2737		4Ir2	0.2794
	2Rh1	0.2878		2Ir1	0.2832
Rh2	2B	0.2134	Ir2	2B	0.2169
	2Mn1	0.2506		2Mn1	0.2401
	1Rh1	0.2737		2Ir2	0.2743
	2Mn2	0.2767		2Mn2	0.2747
	1Rh2	0.2855		1Ir1	0.2794
	2Rh2	0.2878		2Ir2	0.2832
	2Mn1	0.2878		2Mn2	0.2863
	2Rh2	0.2902		2Ir2	0.2980

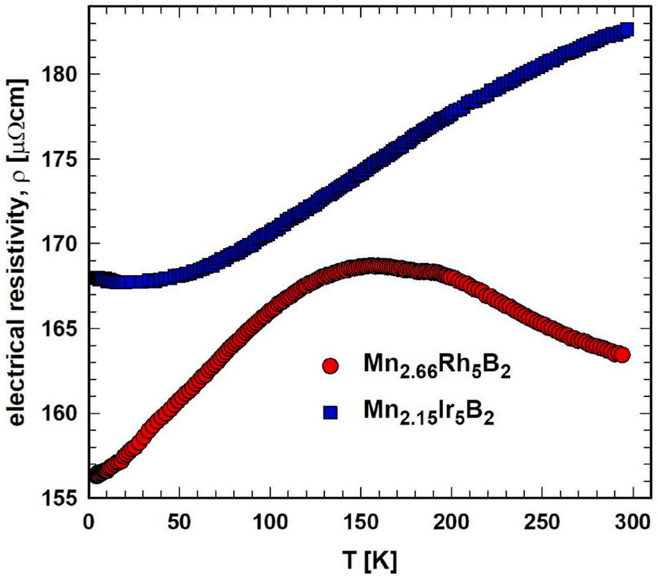

Fig. 3. Temperature dependent electrical resistivity, ρ(T), of $Mn_{2.66}Rh_5B_2$ and $Mn_{2.15}Ir_5B_2$.

0.854 (SC-data) to $a = 0.92030(2)$ nm, $c = 0.279087(9)$ nm for a 3-phase sample Mn33Ir33B34 (in at.%). Although these values are still somewhat smaller than those reported recently (a = 0. 9332(1) nm, c = 0.2896(2) nm [23]), they document the trend in filling the 2a site. A similar observation also holds for $Mn_{3-x}Rh_5B_2$.

It is interesting to note that for $Ti_3Co_5B_2$ large electropositive elements generally were observed to fill the larger units (cubes and pentagonal prisms), whereas the more electronegative and smaller atoms form the framework. In our case manganese atoms qualify for both features being the larger and more electropositive element with respect to the smaller and more electronegative Rh,Ir metal atoms.

Interatomic distances of $Mn_{3-x}\{Rh,Ir\}_5B_2$ in Table 1b reflect the fact that the atoms of Rh and Ir are practically of the same size. Most of the distances in Table 1b comply with the sum of the radii (R_{Rh} = 0.1345 nm, R_{Ir} = 0.1357 nm and R_B = 0.088 nm [36]). This is particularly true for the metal to boron distances at $0.2134 \leq d_{Rh(Ir)–B} \leq 0.220$ nm. The only short distances are encountered for the defect Mn1-site at the centers of the Rh(Ir)-cuboids: $d_{Mn1\text{-}Rh(Ir)} \sim 0.245$ nm.

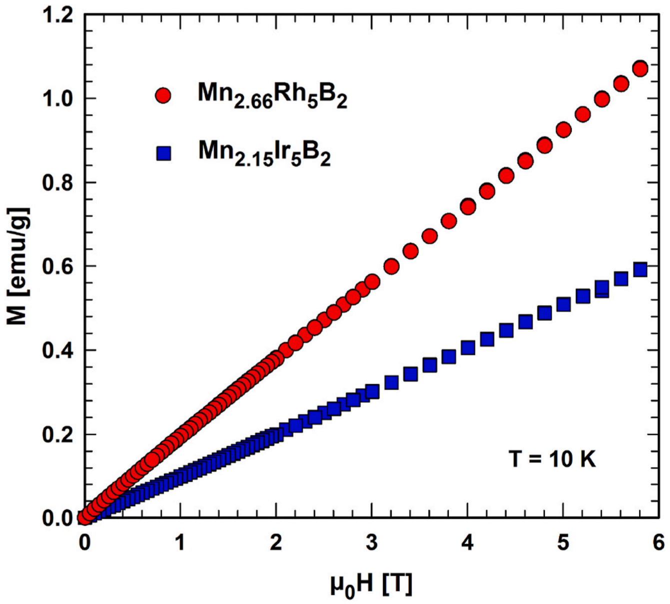

Fig. 4. Field dependent isothermal magnetization of $Mn_{3-x}\{Rh,Ir\}_5B_2$ at 10 K.

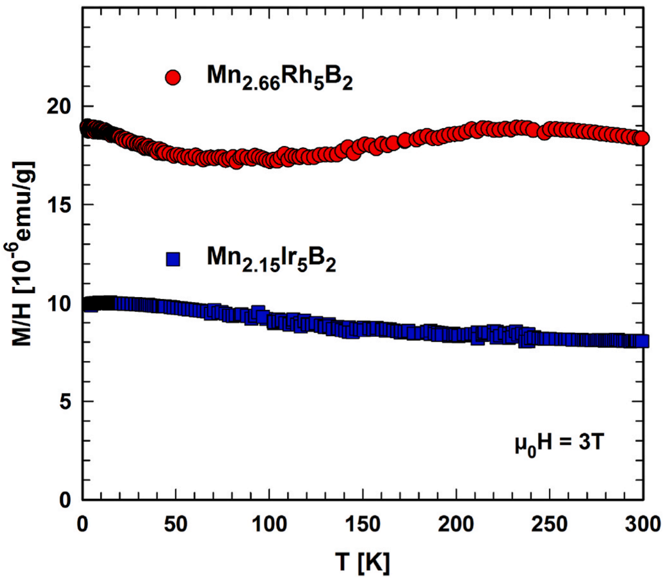

Fig. 5. Magnetic susceptibility, $\chi(T) \equiv M(T)/H$ of $Mn_{3-x}\{Rh,Ir\}_5B_2$ at $\mu_0 H = 3$ T.

3.2. *Physical properties*

Physical properties have been measured on polycrystalline samples, which were shaped by a slow-speed diamond saw from arc-melted specimens, heat treated at 950 °C for about 150 h and quenched.

3.2.1. *Electrical resistivity of $Mn_{3-x}\{Rh,Ir\}_5B_2$*

Fig. 3 summarizes the temperature dependent electrical resistivities, ρ(T), of $Mn_{2.66}Rh_5B_2$ and $Mn_{2.15}Ir_5B_2$, which are dominated by a temperature independent contribution due to potential scattering of conduction electrons by lattice defects. The latter are primarily Mn vacancies at 2a lattice sites (see section 3.1). Minor temperature dependent contributions are metallic-like in the case of $Mn_{2.15}Ir_5B_2$,

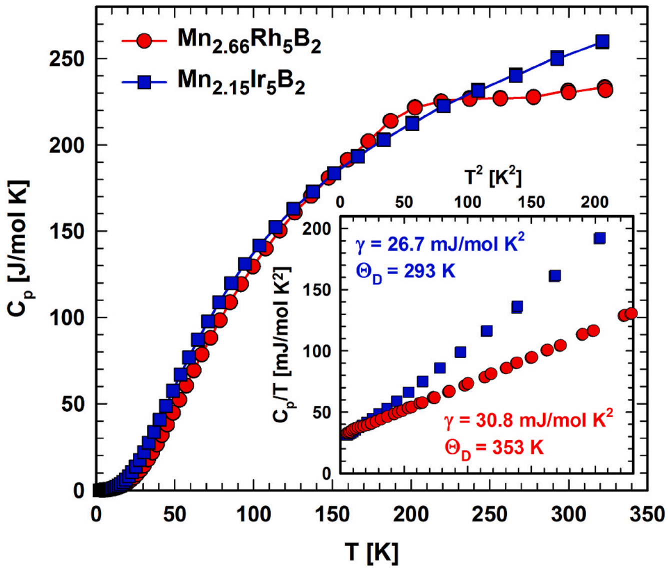

Fig. 6. Temperature dependence of the specific heat for $Mn_{2.66}Rh_5B_2$ and $Mn_{2.15}Ir_5B_2$. Inserts depict C_p/T vs T^2.

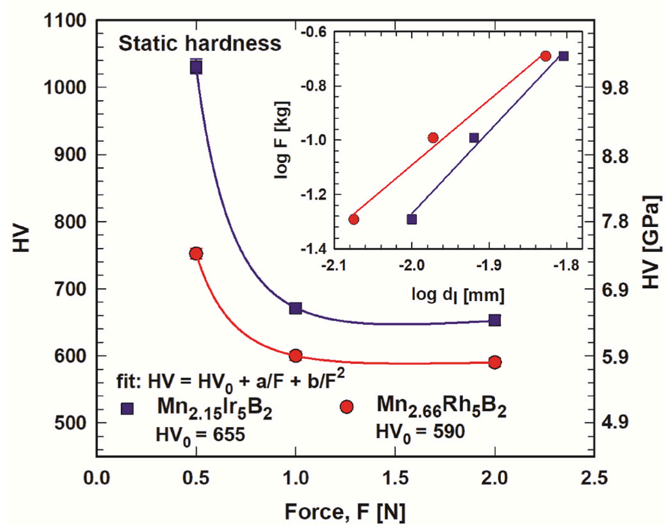

Fig. 7. Vickers hardness as a function of load for $Mn_{2.66}Rh_5B_2$ and $Mn_{2.15}Ir_5B_2$.

whereas in the case of $Mn_{2.66}Rh_5B_2$, ρ(T) displays a non-monotonous temperature dependence with a maximum at around 150 K and a small anomaly at around 190 K, which is probably a signature of a magnetic ordering (for details see below).

3.2.2. *Magnetism of $Mn_{3-x}\{Rh,Ir\}_5B_2$*

Field dependent isothermal magnetization measurements of $Mn_{3-x}\{Rh,Ir\}_5B_2$ taken at 10 K are shown in Fig. 4 and reveal an essentially linear *M*(*H*) behavior, which refers to either a paramagnetic or antiferromagnetic behavior. Accordingly, we compare in Fig. 5 the magnetic susceptibility, $\chi(T) \equiv M(T)/H$ obtained at $\mu_0H = 3$ T, which reveals a weak temperature dependent behavior with a tilde shape of $\chi(T)$ of $Mn_{3-x}Rh_5B_2$, which may indicate a broad antiferromagnetic transition, while for $Mn_{3-x}Ir_5B_2$ $\chi(T)$ displays a simple monotonous decrease as function of temperature which is characteristic of a paramagnetic state.

3.2.3. *Specific heat of $Mn_{3-x}\{Rh,Ir\}_5B_2$*

The temperature dependence of the specific heat of $Mn_{3-x}\{Rh,Ir\}_5B_2$, shown in Fig. 6, reveals a normal metallic low temperature behavior, $C_p(T) = \gamma T + \beta T^3$, which is obvious from the linear trend in a C_p/T vs. T^2 representation of the data shown in the insert of Fig. 6 and yields moderately enhanced Sommerfeld coefficients, γ = 30.8 (1) mJ/mol K^2 and γ = 26.7 (1) mJ/mol K^2 as well as low temperature Debye temperatures, $\theta_D = (12\pi^4 nR/5\beta)^{1/3} = 353$ (2) K and 293 (1) K, for $Mn_{3-x}Rh_5B_2$ and $Mn_{3-x}Ir_5B_2$, respectively. At elevated temperatures of about 200–250 K, $C_p(T)$ of $Mn_{2.66}Rh_5B_2$ displays an unusual bump, which is not observed for $Mn_{2.16}Ir_5B_2$. The broad specific heat anomaly of $Mn_{3-x}Rh_5B_2$ and corresponding anomalies of the electrical resistivity and magnetic susceptibility are indicative of an antiferromagnetic phase transition, which appears to be broadened by lattice disorder related to Mn vacancies. The even larger Mn deficiency of $Mn_{2.16}Ir_5B_2$ may inhibit the formation of long-range magnetic order. Simple estimates of the electronic density of states $N(E_F)$ via the basic Sommerfeld relation, $\gamma = (1/3)\pi^2 k_B^2 N(E_F)$, yield $N(E_F) = 13.1$ and 11.3 states/(eV f.u.) for $Mn_{3-x}Rh_5B_2$ and $Mn_{3-x}Ir_5B_2$, respectively. The corresponding theoretical bare Pauli susceptibilities, $\chi_{Pauli} = \mu_0\mu_B^2 N(E_F)$, thus, result to $\chi_{Pauli} = 0.422\times10^{-3}$ and 0.366×10^{-3} emu/mol for $Mn_{3-x}Rh_5B_2$ and $Mn_{3-x}Ir_5B_2$, respectively. The experimentally obtained values of the magnetic susceptibility are $\chi_{exp} = 12.8\times10^{-3}$ and 11.2×10^{-3} emu/mol for $Mn_{3-x}Rh_5B_2$ and $Mn_{3-x}Ir_5B_2$, respectively, i.e. in rather similar relations of their magnitudes as the experimental Sommerfeld coefficients, in absolute values, however, appear largely enhanced by a factor of about 30 as compared to the estimates of the bare Pauli susceptibilities.

4. Mechanical properties of $Mn_{3-x}\{Rh,Ir\}_5B_2$

As can be seen in Fig. 7, generally the static Vickers hardness HV (load-independent) is lower for $Mn_{2.66}Rh_5B_2$ (HV = 590 ≅ 5.79 GPa) than for $Mn_{2.15}Ir_5B_2$ (HV = 655 ≅ 6.42 GPa) and is increasing with decreasing applied force, indicating an indentation size effect (ISE). To determine ISE, the most widely used empirical equation was applied, i.e. Meyer's law, which gives the correlation between the test load, F, and the resultant indentation size, d_I as $F = k \times d_I^n$, resulting in $\log F = \log k + n \log d_I$. In this equation k is the material constant or power fit and is related to the resistance of a material to penetration, and the exponent n is the size effect index (Meyer's index) and considered as a measure of ISE. For $Mn_{2.15}Ir_5B_2$ n = 3.0, for $Mn_{2.66}Rh_5B_2$ n is slightly lower with n = 2.4 with k = 4.7 N/mm^2 and k = 3.7 N/mm^2, respectively. It is worth mentioning that the ISE is usually related to the deviation of the n-value from n equal to two; n = 2 indicates the absence of an ISE, resulting in hardness values independent of the applied force. The analysis results for both compounds show that ISE is more pronounced for $Mn_{2.15}Ir_5B_2$ than for $Mn_{2.66}Rh_5B_2$.

As explained in the experimental part, RUS was applied to determine the Young's modulus, E, and Poisson's ratio, ν. Due to the fact that microstructures of the melted samples are not homogeneous with respect to bigger and smaller crystals, for both samples it was only possible to get E: for $Mn_{2.15}Ir_5B_2$ E ~210 GPa, for $Mn_{2.66}Rh_5B_2$ E ~170 GPa, respectively.

The sample $Mn_{2.15}Ir_5B_2$, in contrast to $Mn_{2.66}Rh_5B_2$ showed for 1 N load crack propagation in at least ten cases, therefore the indentation fracture toughness could be calculated resulting in an average value of $IK_C = 0.71 \pm 0.5$ MPa $m^{1/2}$.

5. Conclusion

The present paper provides a detailed crystal structure analysis by X-xay single crystal and TEM data for two ternary compounds, $Mn_{3-x}\{Rh,Ir\}_5B_2$, which are isotypic with the $Ti_3Co_5B_2$-type (space group *P*4/*mbm*, No. 127). Characteristic for both compounds is a defect 2*a* site at the origin of the unit cell, however, transmission electron microscopy studies confirm the absence of a superstructure. Various occupancies of the 2*a*-site (M + vac., Mn + B, B + vac., etc.), have been tested, all resulting in indifferent atom parameters, R-values and residual peaks. A study of the phase equilibria around the two phases at 950 °C, $Mn_{3-x}Rh_5B_2$ (x~0.34) and $Mn_{3-x}Ir_5B_2$

(x~0.85), shows rather limited homogeneity regions pointing towards slightly higher Mn-contents. Physical property studies (on polycrystalline material) as a function of temperature (below RT; specific heat, electrical resistivity, magnetization) reveal for $Mn_{2.66}Rh_5B_2$ signatures of an antiferromagnetic phase transition near 200 K and a plain metallic-like behavior for $Mn_{2.15}Ir_5B_2$. Both borides are brittle with elastic moduli and Poisson's ratio determined at room temperature from Resonant Ultrasonic Spectroscopy (RUS) data, yielding Young's moduli of $E \sim 170$ GPa for $Mn_{2.66}Rh_5B_2$ and $E \sim 210$ GPa for $Mn_{2.15}Ir_5B_2$. Vickers hardness HV is lower for $Mn_{2.66}Rh_5B_2$ ($HV = 590 \cong 5.79$ GPa) than for $Mn_{2.15}Ir_5B_2$ ($HV = 655 \cong 6.42$ GPa). The indentation fracture toughness was $IK_C = 0.71 \pm 0.5$ MPa $m^{1/2}$.

CRediT authorship contribution statement

Gerda Rogl: Investigation, Validation. **Markus Eiberger:** Investigation, Validation. **Soner Steiner:** Investigation. **Herwig Michor:** Investigation, Validation, Writing – review & editing. **Jiri Bursik:** Investigation, Validation. **Gerald Giester:** Investigation. **Andrij Grytsiv:** Investigation. **Peter F. Rogl:** Conceptualization, Investigation, Supervision, Validation, Writing – original draft, Writing – review & editing.

Declaration of competing interest

I herewith state that for the submitted research manuscript with title "Borides $Mn_{3-x}\{Rh,Ir\}_5B_2$ with $Ti_3Co_5B_2$-type: X-ray single crystal and TEM data, physical properties", authored by Gerda Rogl, Markus Eiberger, Soner Steiner, Herwig Michor, Jiri Bursik, Gerald Giester, Andrij Grytsiv, Peter F. Rogl, no conflicts of interest exist.

Data availability

Data will be made available on request.

Acknowledgements

The research reported herein was in part supported by the Austrian OEAD within the WTZ-project Austria-Czech Republic, project no. CZ-01/2019. We thank Dr. S. Puchegger for his expert assistance in EPMA and RUS measurements.

Appendix A. Supplementary data

Supplementary data to this article can be found online at https://doi.org/10.1016/j.solidstatesciences.2024.107583.

References

[1] Q. Gu, G. Krauss, W. Steurer, Transition metal borides: superhard versus ultra incompressible, Adv. Mater. 20 (2008) 3620–3626.
[2] J.B. Levine, S.L. Nguyen, S.E. Brown, H.I. Rasool, R.B. Kaner, J.A. Wright, Preparation and properties of metallic, superhard Rhenium diboride crystals, J. Am. Chem. Soc. 130 (2008) 16953–16958.
[3] R.F. Zhang, D. Legut, Z.J. Lin, Y.S. Zhao, H.K. Mao, S. Veprek, Stability and strength of transition-metal tetraborides and triborides, Phys. Rev. Lett. 108 (2012) 255502.
[4] G. Akopov, L.E. Pangilinan, R. Mohammadi, R.B. Kaner, Perspective: superhard metal borides: a look forward, Apl. Mater. 6 (7) (2018) 1–8, 070901.
[5] M. Xie, High pressure studies of ultra-incompressible, superhard metal borides 75 (3E) (2013) 145.
[6] S. Zhang, Z. Wang, P. Guo, P. Ke, M. Oden, A. Wang, Temperature induced superhard CrB_2 coatings with preferred (001) orientation deposited by DC magnetron sputtering technique, Surf. Coating. Technol. 322 (2017) 134–140.
[7] I. Pinter, Method and composition of materials for making wear resistant surface coating, PCT Int. Appl. WO (2005), 2005121402 A1 20051222.
[8] S. Hirosawa, Permanent magnets beyond Nd- Dy- Fe- B, IEEE Trans. on Magnetics 55 (2, Pt. 1) (2019) 1–6, 2100506.
[9] D. Li, Y. Li, D. Pan, Z. Zhang, Ch-J. Choi, Prospect and status of iron- based rare-earth- free permanent magnetic materials, J. Magn. Magn Mater. 469 (2019) 535–544.
[10] R. Hott, R. Kleiner, T. Wolf, G. Zwicknagl, Review on superconducting materials, from arXiv.org, e-Print Archive, Condensed Matter (2013) 1–50, arXiv: 1306.0429v1 [cond-mat.supr-con].
[11] E. Bauer, M. Sigrist, Non-Centrosymmetric superconductors: Introduction and overview, in: Lecture Notes in Physics, vol. 847, Springer-Verlag, Berlin, 2012.
[12] A.A. Aczel, T.J. Williams, T. Goko, J.P. Carlo, W. Yu, Y.J. Uemura, T. Klimczuk, J. D. Thompson, R.J. Cava, G.M. Luke, Muon spin rotation/relaxation measurements of the noncentrosymmetric superconductor $Mg_{10}Ir_{19}B_{16}$, Phys. Rev. B: Cond. Matter and Materials Physics 82 (2) (2010) 1–6, 024520.
[13] P. Thalmeier, A. Akbari, Resonant spin excitations in unconventional heavy fermion superconductors and Kondo lattice compounds, From arXiv.org, e-Print Archive, Condensed Matter (2014) 1–34, arXiv:1412.2523v1.
[14] M.S. Grbic, E.C.T. O'Farrell, Y. Matsumoto, K. Kuga, M. Brando, R. Kuechler, A. H. Nevidomskyy, M. Yoshida, T. Sakakibara, Y. Kono, Quantum critical behavior and Lifshitz transition in intermediate valence α- $YbAlB_4$, from arXiv.org, e-Print Archive, Condensed Matter (2019) 1–18.
[15] H.C. Ku, R.N. Shelton, Re-entrant superconductivity in the orthorhombic system thulium lutetium ruthenium boride ($(Tm_{1-x}Lu_x)RuB_2$, Solid State Commun. 40 (3) (1981) 237–240.
[16] E. Lee, B.P.T. Fokwa, Nonprecious metal borides: emerging electrocatalysts for hydrogen production, Acc. Chem. Res. 55 (2021) 56–64.
[17] P. Rogl, Existence and crystal chemistry of borides, in: J.J. Zuckerman, A.P. Hagen (Eds.), Inorganic Reactions and Methods, vol. 13, VCH-Publications Inc., New York, 1991, pp. 85–167 (chapter 6).7.
[18] B.P.T. Fokwa, Borides: Solid-State Chemistry, vols. 1–14, Encyclopedia of Inorganic and Bioinorganic Chemistry, 2014.
[19] D. Hobbs, J. Hafner, D. Spisak, Understanding the complex metallic element Mn. I. Crystalline and noncollinear magnetic structure of α- Mn, Phys. Rev. B: Condensed Matter and Materials Physics 68 (1) (2003) 1–18. ; see also J. Hafner, D. Hobbs, Understanding the complex metallic element Mn. II. Geometric frustration in β-Mn, phase stability, and phase transitions, Phys. Rev. B: Condensed Matter and Materials Physics, 68(1), 014408, 1–15 (2003); and M. Zeleny, M. Sob, J. Hafner, Noncollinear magnetism in manganese nanostructures, Phys. Rev. B: Condensed Matter and Materials Physics, 80(14), 1–9 (2009).
[20] P. Shankhari, Y. Zhang, D. Stekovic, E.M. Itkis, B.P.T. Fokwa, Unexpected competition between antiferromagnetic and ferromagnetic states in $Hf_2MnRu_5B_2$: predicted and realized, Inorg. Chem. 56 (21) (2017) 12674–12677.
[21] Y. Zhang, G.J. Miller, B.P.T. Fokwa, Computational design of rare-earth-free magnets with the $Ti_3Co_5B_2$-type structure, Chem. Mater. 29 (6) (2017) 2535–2541.
[22] Y. Zhang, B.P.T. Fokwa, Density Functional Investigation on the Magnetic Anisotropy in Rare-earth-free Metal Borides with the $Ti_3Co_5B_2$-type Structure, from Abstracts of Papers, 253rd ACS National Meeting & Exposition, San Francisco, CA, United States, 2017.
[23] B. Petermüller, C. Neun, M. Stekiel, D. Zimmer, M. Tribus, K. Wurst, B. Winkler, H. Huppertz, Synthesis, crystal structure, and compressibilities of $Mn_{3-x}Ir_5B_{2+x}$ ($0 \leq x \leq 0.5$) and Mn_2IrB_2, Chem. Eur J. 24 (2018) 14679–14685.
[24] S. Steiner, G. Rogl, M. Eiberger, H. Michor, J. Bursik, G. Giester., A. Grytsiv, P.F. Rogl, A DFT Study of Mn3-x$\{Rh,Ir\}_5B_2$, to be published.
[25] J. Rodriguez-Carvajal, FULLPROF, a program for Rietveld refinement and pattern matching analysis, abstract of the satellite meeting on powder diffraction of the XV congress, 1990, p. 127, int. Union of crystallography, talence, France. See also: recent developments of the program FULLPROF, Comm. Powder Diffr. IUCr. Newsl. 26 (2001) 12–19.
[26] Bruker Advanced X-ray solutions. APEX2 User Manual. Version 1.22. 2004, Bruker AXS Inc. For APEXII, SAINT and SADABS see 2008, Bruker Analytical X-ray Instruments, Inc., Madison, Wisconsin, USA.
[27] G.M. Sheldrick, SHELX – program for crystal structure refinement, Acta Crystallogr, CrystEngComm 6 (2004) 303–309. A64 (2008) 112-122; Windows version OSCAIL by P. McArdle, K. Gilligan, D. Cunningham, R. Dark, M. Mahon.
[28] E. Parthé, L. Gelato, B. Chabot, M. Penzo, K. Censual, R. Gladyshevskii, TYPIX – standardized data and crystal chemical characterization of inorganic structure types 1994 (Berlin, Heidelberg: springer-Verlag) see also, J. Appl. Crystallogr. 20 (1987) 139–143.
[29] A.L. Spek, Single-crystal structure validation with the program PLATON, J. Appl. Crystallogr. 36 (2003) 7–11.
[30] P.A. Stadelmann, JEMS: Java Electron Microscopy Software, 2024. Switzerland, http://www.jems-swiss.ch.
[31] P.A. Stadelmann, EMS - a software package for electron diffraction analysis and HREM image simulation in materials science, Ultramicroscopy 21 (1987) 131–145.
[32] P. Villars, K. Censual, Pearson's Crystal Data: Crystal Structure Database for Inorganic Compounds, ASM International, Materials Park: Ohio, USA, Release 2021/22.
[33] ICSD Database 2018/2: (Fachinformationszentrum Karlsruhe, Germany).
[34] Y.B. Kuz'ma, Y.P. Yarmolyuk, Crystalline structure of the compound $Ti_3Co_5B_2$, J. Struct. Chem. 12 (1971) 422–424, translated from Zh. Strukt. Khim. 12, 458-461 (1971).
[35] B.F.T. Fokwa, M. Hermus, Complete titanium substitution by boron in a tetragonal prism: exploring the complex boride series $Ti_{3-x}Ru_{5-y}Ir_yB_{2+x}$ ($0 \leq x \leq 1$ and $1 < y < 3$) by experiment and theory, Inorgan. Chem. 50 (2011) 3332–3341.
[36] W.B. Pearson, The Crystal Chemistry and Physics of Metals and Alloys, 1972. New York, USA: Wiley-Interscience, The 12-coordinated metallic radii in Table 4-4 of this book have been taken from: E. Teatum, K. Gschneidner, and J. Waber, Report LA-2345, US Department of Commerce, Washington, D.C., USA, 1960.